



# Deformation mechanisms of antigorite serpentinite at subduction zone conditions determined from experimentally and naturally deformed rocks

Anne-Line Auzende, Javier Escartin, Nicolas Walte, Stéphane Guillot, Greg Hirth, Daniel J. Frost

## ► To cite this version:

Anne-Line Auzende, Javier Escartin, Nicolas Walte, Stéphane Guillot, Greg Hirth, et al.. Deformation mechanisms of antigorite serpentinite at subduction zone conditions determined from experimentally and naturally deformed rocks. *Earth and Planetary Science Letters*, Elsevier, 2015, 411, pp.229-240. <10.1016/j.epsl.2014.11.053>. <hal-01110205>

**HAL Id: hal-01110205**

**<http://hal.upmc.fr/hal-01110205>**

Submitted on 27 Jan 2015

**HAL** is a multi-disciplinary open access archive for the deposit and dissemination of scientific research documents, whether they are published or not. The documents may come from teaching and research institutions in France or abroad, or from public or private research centers.

L'archive ouverte pluridisciplinaire **HAL**, est destinée au dépôt et à la diffusion de documents scientifiques de niveau recherche, publiés ou non, émanant des établissements d'enseignement et de recherche français ou étrangers, des laboratoires publics ou privés.



1 Deformation mechanisms of antigorite serpentinite at subduction zone  
2 conditions determined from experimentally and naturally deformed rocks

3  
4  
5 Anne-Line Auzende<sup>1, now 4</sup>, Javier Escartin<sup>2</sup>, Nicolas Walte<sup>3</sup>, Stéphane Guillot<sup>4</sup>, Greg Hirth<sup>5</sup>,  
6 Daniel J. Frost<sup>3</sup>

7  
8  
9  
10 <sup>1</sup> IMPMC, Universités Paris Diderot & Paris 06, UMR CNRS 7590, MNHN, IRD UMR 206 4  
11 place Jussieu, F75005 Paris, France

12 <sup>2</sup> CNRS, IPGP, 1 rue Jussieu, 75238 Paris, France

13 <sup>3</sup> Bayerisches Geoinstitut, Universität Bayreuth, Universitätsstraße 30, 95447 Bayreuth,  
14 Germany

15 <sup>4</sup> ISTERRE, CNRS, Université Grenoble Alpes, 38000 Grenoble, France

16 <sup>5</sup> Department of Geological Sciences, Brown University, 324 Brook Street, Box 1846  
17 Providence, RI 02912, USA

18  
19 **Corresponding author** : Anne-Line Auzende

20 phone : +33(0)4 76 51 40 66

21 Email : anne-line.auzende@ujf-grenoble.fr

22  
23 key words : antigorite, serpentine minerals, Deformation DIA, fluid migration, brittle,  
24 subduction zone

25 **Abstract**

26 Deformation-DIA experiments on antigorite serpentinite were performed at pressures of 1-3.5  
27 GPa and temperatures of between 400 and 650°C, bracketing the stability of antigorite under  
28 subduction zone conditions. For each set of pressure-temperature (P-T) conditions, we  
29 performed two runs at strain rates of  $5 \times 10^{-5}$  and  $1 \times 10^{-4} \text{ s}^{-1}$ . We complemented our study with  
30 a sample deformed in a Griggs-type apparatus at 1 GPa and 400°C (Chernak & Hirth, 2010),  
31 and with natural samples from Cuba and the Alps deformed under blueschist/eclogitic  
32 conditions. Optical and transmission electron microscopy were used for microstructural  
33 characterization and determination of deformation mechanisms. Our observations on  
34 experimentally deformed antigorite prior to breakdown show that deformation is dominated  
35 by cataclastic flow with a minor but perceptible contribution of plastic deformation  
36 (microkinking and (001) gliding mainly expressed by stacking disorder mainly). In contrast,  
37 in naturally deformed samples, deformation-related plastic structures largely dominate  
38 (stacking disorder, kinking, pressure solution), with minor but also perceptible contribution of  
39 brittle deformation. When dehydration occurs in experiments, plasticity increases and is  
40 coupled to local embrittlement attributed to antigorite dehydration. In dehydrating samples  
41 collected in the Alps, embrittlement is also observed suggesting that dehydration can  
42 contribute to intermediate-depth seismicity. Our results thus show that semibrittle deformation  
43 operates within and above the stability field of antigorite. However, naturally deformed  
44 samples record primarily plastic deformation that likely take places at low strain rates. We  
45 also document that the corrugated structure of antigorite has a control on the strain  
46 accommodation mechanisms under subduction conditions, with preferred inter and intra-grain  
47 cracking along (001) and gliding along both *a* and *b*. We also show that antigorite rheology in  
48 subduction zones is partly controlled by the presence of fluids, which can percolate within the  
49 exhumation channel via deformation-induced interconnected porosity.

50 **1. Introduction**

51

52 Subduction zones are the setting of numerous processes that impact the dynamics and  
53 geochemical evolution of the Earth (see Tatsumi & Kogiso, 2003; Hirth & Guillot, 2013). In a  
54 context where tectonic stresses dominate, the peculiar rheological properties of serpentinites  
55 focus the interest of the scientific community (see Reynard, 2013 for a review). Indeed,  
56 serpentinites are believed to be an important component of the subducting slab owing to the  
57 hydrothermal alteration of the oceanic lithosphere (Mevel, 2003; Garth and Rietbrock, 2014).  
58 Additionally, serpentinite are present in the mantle wedge due to fluids rising from the  
59 dehydrating lithosphere, as inferred from the low seismic velocities (Hyndman & Peacock,  
60 2003) and the high Poisson's ratio (Kamiya & Kobayasi, 2000) measured in the mantle  
61 wedge. These inferences from geophysical observations are supported by field evidence in  
62 paleo-subduction zones (Guillot et al, 2009) or serpentine mud volcanoes (Fryer et al, 1999).  
63 Understanding how serpentinites deform in subduction zones, particularly in the exhumation  
64 channel that overlies the subducting slab (Hilairret & Reynard, 2009), is of prime importance  
65 to understand decoupling between the downwelling slab and the overriding plate (Wada et al,  
66 2008), exhumation of high-pressure rocks (Guillot et al, 2001; Agard et al, 2009), controls on  
67 fluids pathways (Padrón-Navarta et a, 2010) and, more generally, the mantle wedge dynamics  
68 (see van Keken, 2003 and references therein). Also, when serpentine breaks down at depth,  
69 the embrittlement caused by the migration of dehydration fluids is believed to trigger  
70 seismicity (Dobson et al, 2002; Hacker et al, 2003; Jung & Green, 2004; Peacock, 2001;  
71 Garth and Rietbrock, 2014). The fate of the dehydration fluids is also of great importance as  
72 they affect the properties of mantle rocks such as their rheology and melting temperature and  
73 the geochemical budget of elements that are recycled in the subduction zone (Deschamps et  
74 al, 2013; Marchesi et al, 2013).

75           Serpentine minerals, which are 1:1 hydrous phyllosilicates, display three main  
76 structural varieties: lizardite (flat), chrysotile (tubular), and antigorite (corrugated). In  
77 subduction zones, antigorite is the stable serpentine variety (Ulmer & Trommsdorff, 1995)  
78 and its rheological behaviour has been probed by numerous experimental studies, yielding  
79 diverging results or interpretations. Some experimental studies document deformation in the  
80 (semi-) brittle regime (Escartin et al, 1997; Jung & Green, 2004; Chernak and Hirth, 2010),  
81 while at similar deformation conditions other studies suggest that deformation operates in the  
82 plastic regime (Hilaireret et al., 2007). As models of mantle wedge dynamics and fluid transport  
83 feed from these experimental data, it is necessary to better constrain and understand the  
84 precise mode of deformation of antigorite within the subduction zone, and in particular  
85 around dehydration conditions. For this purpose, we conducted experiments with a  
86 Deformation-DIA apparatus, at strain rates and total strains similar to those reported in  
87 previous studies, and coupled this experimental study with the investigation of naturally  
88 deformed samples. To facilitate the comparison of experimentally and naturally deformed  
89 rocks, we conducted experiments under P-T conditions similar to the metamorphic conditions  
90 experienced by serpentinites from the Alps and Cuba (**Figure 1**). The microstructures of the  
91 samples described in this study (from a few  $\mu\text{m}$  to nm) were investigated with optical and  
92 transmission electron microscopy (TEM) to determine and interpret deformation mechanisms.  
93 Microstructural observations are indeed the key way to infer, at the micron scale, the strain  
94 accommodation processes of minerals (see Passchier and Throw, 2005), particularly for  
95 phyllosilicates (Shea and Kronenberg, 1992). Investigating both field and laboratory samples  
96 is essential in order to constrain the application field of experiments, which necessarily lack  
97 the complexity of natural systems as well as their duration. Furthermore, differences between  
98 experimental and natural microstructures should highlight the effect(s) and importance of  
99 processes not active in experiments.

## 100 **2. Materials and methods**

101

### 102 **2.1. Experimental deformation**

#### 103 *Experimental device*

104 The D-DIA high-pressure experiments were carried out at the Bayerisches Geoinstitut  
105 (Bayreuth, Germany). This device is based on a DIA cubic anvil apparatus that consists of  
106 symmetric upper and lower blocks, four wedge-shaped thrust blocks and six anvils. The  
107 square truncations of the anvils define a cubic volume in which the high-pressure cell  
108 assembly containing the sample is loaded (**Figure 2**). The D-DIA is capable of generating  
109 pressures up to 10 GPa at high temperatures (up to 2000°C), and then deforming the sample.  
110 Hydrostatic pressure is reached at room temperature by closing up concurrently the anvils  
111 with a rate of 0.02 GPa/min. Once a high pressure is attained, temperature is increased with a  
112 heating-resistance furnace made of LaCrO<sub>3</sub>, with temperature ramping up between 50 and  
113 100°C/min. Temperature was determined using a W-Re thermocouple inserted axially into the  
114 assembly and in contact with the top of the sample. When the required P and T are achieved,  
115 the sample is annealed for a couple of hours to remove the eventual deformation-induced  
116 structures acquired during cold compression. After annealing, the samples were deformed by  
117 controlled shortening of the vertical anvil axis, which induced axial compression in the  
118 cylindrical samples while keeping the confining pressure constant. Total time at high  
119 temperature is ranging between about 180 ( $1 \times 10^{-4} \text{ s}^{-1}$ ) and 240 min ( $5 \times 10^{-5} \text{ s}^{-1}$ ). The  
120 deformation is monitored with displacement transducers. Strain and strain rate can thus be  
121 controlled, and are reported for each experimental run in table 1.

122 After quenching the sample at the end of the experiment, special care was taken to  
123 unload the sample and prevent brittle deformation structures during decompression. The  
124 retraction of the upper and lower anvils was continuously adjusted to achieve comparable

125 displacements to those of the four lateral anvils. For further details, the configuration of the  
126 D-DIA is described by Wang et al. (2003).

127 Experimental conditions are presented in **Table 1** and **Figure 1**. Pressure and  
128 temperature conditions reflect the HP-LT conditions experienced by natural serpentinites  
129 from the Monviso and Erro Tobbio Massif in the Alps (Schwartz et al, 2000; Scambelluri et  
130 al, 1995; Angiboust et al, 2011) or from Cuba (Auzende et al, 2002). They also compare well  
131 to experiments by Chernak et al (2010) conducted in a Griggs-type apparatus; Chernak et al.'s  
132 (2010) sample W1460, deformed at 1 GPa and 400°C was provided by the authors in order to  
133 conduct microstructural analyses as part of this study. The deformation experiments by  
134 Hilairet et al (2007) were performed along a colder geotherm, and included several loading  
135 and unloading cycles at different strain rates. We performed systematically two experiments  
136 under each set of P-T conditions, but at different strain-rates (see Table 1). Each sample was  
137 therefore deformed in a single deformation event at a single P and T and subsequently  
138 quenched. To document possible deformation structures induced by compression or  
139 decompression, one static experiment, DD63, was pressurized at 1.8 GPa and 550°C,  
140 annealed for two hours and then quenched and decompressed. The P-T conditions of the static  
141 experiment correspond to deformation experiments DD64 and DD65 (**Table 1**).

142

#### 143 *Starting material*

144 The starting material was a natural serpentinite collected in the Monviso ophiolite unit  
145 (Western Alps, Italy). Originally an oceanic mantle lithosphere, the unit was buried during  
146 alpine subduction and underwent HP-LT metamorphic conditions under eclogite facies  
147 conditions. The sample, taken from a preserved lens embedded within a highly sheared matrix  
148 of serpentinites, is fully serpentitized, without trace of inherited minerals such as olivine or  
149 pyroxene (sample 627-1, see Auzende *et al.*, 2006). The serpentine chemistry lies within the

150 normal range of antigorite composition with little aluminium ( $\text{Al}_2\text{O}_3=1.97\text{wt}\%$ ) and iron  
151 ( $\text{FeO}_t=2.46\text{ wt}\%$ ), and the petrological investigation shows that the sample consists almost  
152 exclusively of antigorite blades up to several tens of  $\mu\text{m}$  in length, associated with magnetite.  
153 This sample, massive and unfoliated at the macroscopic scale, displays under a light  
154 microscope a typical interpenetrative texture with no preferred orientation and without  
155 noticeable deformation-induced structures under a light microscope (no crystallographic  
156 preferred orientation, thereafter referred as CPO), as shown on **Figure 3a**. TEM  
157 characterisation of this sample shows crosscutting antigorite blades, displayed on **Figure 3b**.  
158 Furthermore, at this nanoscale, no significant evidence of deformation was observed either.

159 For experiments, cylindrical cores 1.4 mm in diameter, and 1.6 mm in length were  
160 drilled in the bulk rock, and loaded in the D-DIA assembly designed for high-pressure  
161 experiments, as presented in **Figure 2a**. Materials constituting the assembly have been chosen  
162 for their physical (e.g., compression modulus) and chemical properties (no reaction with the  
163 sample) at experimental conditions.

164

## 165 **2.2. Naturally-deformed samples**

166 Sheared serpentinites are common in nature, but their deformation is often linked to  
167 retrograde, low P-T conditions. Instead, we have selected sheared serpentinite samples with  
168 inferred deformation occurring during prograde or peak metamorphic conditions (see Table  
169 1), to facilitate comparison with experimental results.

170 Samples Cu12 and Cu24 sample were collected in the Escambray massif (Cuba) from  
171 an eclogitic unit (Auzende et al, 2002), that deformed at the metamorphic peak conditions  
172 affecting also the associated eclogitic metabasite, which shows a paragenesis consisting of  
173 almandine garnet + omphacite ( $\text{Jd}_{40}$ )  $\pm$  glaucophane + phengite ( $\text{Si} \sim 3.4\text{ pfu}$ ) + paragonite +  
174 zoisite + quartz + rutile. Sample Al24 was collected in the Erro Tobbio unit, in the alpine

175 Voltri massif (Italy), which records different steps of burial during subduction. Hermann et al  
176 (2000) evaluated the metamorphic conditions of unit I (labelled ET1 in Fig.1), where Al24  
177 was collected, at  $P = 0.9 \pm 0.3$  GPa and  $T = 360 \pm 60^\circ\text{C}$ . Deformation structures are  
178 synchronous with prograde metamorphism. Samples Al19 and Al20 (labeled ET3 in Fig.1)  
179 were also collected in the Erro Tobbio unit and underwent more severe metamorphic  
180 conditions, which Hermann et al. (2000) evaluate at  $P = 2.0 \pm 0.2$  GPa and  $600 \pm 40^\circ\text{C}$  (ET3).

181

### 182 **2.3. TEM observations**

183 All samples, natural or experimental, were prepared for microstructural  
184 characterisation using an ion-polishing system, which provides for each sample large thin  
185 sections. Prior to thinning, the experimental cells were embedded in epoxy resin and cut  
186 parallel to the shortening direction with a 20 $\mu\text{m}$ -wire saw. The natural samples were cut  
187 perpendicular to the foliation direction. All samples were glued with Crystal Bond  
188 thermofusible epoxy onto a glass slide, thinned, and polished down to 30  $\mu\text{m}$ . TEM  
189 preparations were optically selected from the polished petrographic sections. A copper slot (1  
190  $\times$  2 mm) was glued to surround each selected area, cored with a razor blade, and removed by  
191 heating the thermofusible epoxy. We used a conventional ion-milling system (PIPS for  
192 precision ion polishing system) with an argon beam operated at 5 kV. Electron transparency  
193 suitable for high-resolution imaging is achieved at the edge of the hole created by the milling  
194 beam. Amorphous zones were removed by decreasing the operating conditions down to 2.5  
195 kV. TEM was performed at IMPMC (Paris, France). Imaging, diffraction and chemical data  
196 were obtained with a JEOL 2100 microscope with a LaB6 filament and a JEOL 2100F with a  
197 field emission gun, both operating at 200kV and equipped with JEOL EDX detectors. Table 2  
198 lists and describes the deformation-related microstructures that were observed in  
199 experimentally and naturally deformed antigorite serpentinites.

## 200 **3. Results**

### 201 **3.1. Experimental deformation**

#### 202 *Static experiment*

203 To discriminate between structures inherited from the starting material and those generated  
204 during compression/decompression, we examined by optical microscopy and TEM both the  
205 starting material and sample DD63, which was statically pressurized to 1.8 GPa and annealed  
206 for two hours at 550°C before temperature quenching and decompression. The petrological  
207 investigation of these two samples shows no significant differences. The original  
208 interpenetrative textures are recognized in the pressurized sample (**Figure 3c**), which displays  
209 intercrystalline cracks that we attribute to cold decompression. TEM observations of the  
210 DD63 sample show large crosscutting antigorite blades typical of interpenetrative textures  
211 and similar to those observed in the starting material (**Figure 3b**). A few chrysotile veins are  
212 observed in both samples, probably inherited from oceanic hydrothermal circulation or late  
213 retrogression of serpentinite 627-1 during exhumation. Based on these observations, we can  
214 assume that pressurization and depressurization do not induce changes to texture beyond the  
215 decompression micro-cracks, which remain open and are easily recognizable in the deformed  
216 samples.

217

#### 218 *Experiments without evidence for dehydration*

219 We conducted experiments under two sets of P-T conditions within the stability field of  
220 antigorite (**Table 1** and **Figure 1**). These conditions reflect those experienced by natural  
221 serpentinites involved in subduction. We report the results obtained on our D-DIA samples  
222 and on sample W4160 provided by L. Chernak. In all samples, decompression cracks sub-  
223 perpendicular the shortening direction are observed (Figure 4b and c) and will not be taken  
224 into account when discussing the deformation-linked microstructures.

225 Observed under a polarized light microscope, the four deformed samples share several  
226 features showing that deformation is not pervasive. The original interpenetrative texture is  
227 well preserved and has a grain size similar to that of the starting material, with antigorite  
228 blades that can reach several tens of micrometers (**Figure 4a**). None of the experimentally  
229 deformed samples display penetrative foliation or schistosity. A few features associated with  
230 localized deformation can however be recognized at this scale. In W1460, a sharp fault  
231 crosscuts the sample at a 45° angle with respect to  $\sigma_1$ , and has an apparent displacement of  
232 about 200  $\mu\text{m}$ . A second type of localization is observed in two samples (DD61, DD65), in  
233 the form of narrow damaged zones (about 10  $\mu\text{m}$  wide) that originate at the corner of the  
234 alumina piston and propagate diagonally throughout the sample (**Figures 2d and 4b**). These  
235 sheared zones propagate at an angle about 30° from  $\sigma_1$  in DD65 and with slightly steeper  
236 angle of ~40° in DD61, and display no apparent displacement (e.g., offset at sample edge).  
237 We attribute these features to an inhomogeneity of the distribution of deformation linked to  
238 the impingement of the piston (stress shadows). These damage zones are not as sharp as the  
239 fault observed in sample W1460 (**Figure 4c**), deformed at conditions similar to DD60 and  
240 DD61. Locally, grains with significant CPO can be observed at the vicinity of the damaged  
241 zones from our D-DIA samples (**Figure 4b**) and along the fault observed in W1460, as  
242 previously described by Chernack et al (2010). This is not a common feature in these samples,  
243 and we attribute it to the fault being locally parallel to pre-existing crystal orientation, and  
244 exploiting optimally oriented grain boundaries at a local scale.

245 We conducted extensive TEM characterization of all deformed samples, and acquired  
246 more than 400 micrographs, which provide a comprehensive overview of nanostructures.  
247 Overall quantification of the various structures (e.g., fracture or dislocation density) observed  
248 in the experimentally deformed samples is not possible, due to the inhomogeneous  
249 distribution of the deformation within each sample and the great difficulty to acquire a

250 sufficiently large set of TEM images to perform statistical analyses. However, our systematic  
251 TEM observations do document clear microstructural patterns. According to these  
252 observations, we do not observe significant differences among samples deformed under  
253 conditions below the antigorite dehydration temperature.

254         Large interpenetrative blades of antigorite, similar to those in the starting material, are  
255 the most widespread texture. Decompression cracks can easily be recognized, as they are  
256 open fractures sub-perpendicular to  $\sigma_1$ . We also document distinctive microstructures that we  
257 can link to experimental deformation. **Figures 5a and b** show grains of antigorite displaying  
258 cataclastic deformation, as indicated by broken-up crystals with sharp edges, a heterogeneous  
259 grain size, and predominant delamination along the basal planes in addition to fractures at  
260 random orientations. This micro-fracturing results in local grain-size reduction and the  
261 development of incipient cataclasite textures arising from local grinding of crystals,  
262 surrounded by sample material that shows a low degree of deformation. These deformation  
263 textures can be observed in all samples, but are particularly common in DD60 and DD61,  
264 deformed at 1 GPa and 400°C. Further evidence of brittle behavior is the occurrence of  
265 intracrystalline fractures (**Figure 5c and d**) that affect large crystals, mainly along the  
266 cleavage planes, or associated with the bending/kinking of antigorite blades. All of these  
267 structures strongly emphasize a brittle behavior of antigorite under the P-T conditions of  
268 subduction, but at experimental strain rates that are high relative to natural strain rates.

269         Coupled to these brittle structures, we also observe features associated with plastic  
270 deformation, such as kinking, as shown in **Figures 5d and e** (DD60 and DD65) and in **Figure**  
271 **5f** (W1460). As observed on the micrographs, gliding occurs in the basal planes along *a* or *b*  
272 directions (**Figure 5d-e** and **Figure 5f** respectively). As shown in the insert of **Figure 5e**,  
273 gliding along *a* is commonly accompanied by significant stacking disorder. Kinking can be  
274 associated with cracks that develop at the hinges of the kinks (F in **Figure 5d**) or with

275 dislocation walls that propagate within the bands (DW in **Figure 5f**). Kink-bands are  
276 observed in all deformed samples, but they are not very abundant and cannot accommodate a  
277 significant amount of the permanent strain. We also noted that in all deformed samples, most  
278 antigorite crystals are well ordered (**Figure 5g**), as observed in the starting material, with a  
279 constant modulation wavelength, and a regular layer stacking. Intracrystalline disorder  
280 (stacking faults, twinning, offset) can be recognized only in some crystals, commonly in those  
281 affected by deformation structures such as kinking (**Figure 5e** - insert), or in crystals in the  
282 vicinity, demonstrating that intra-crystalline defects are deformation-related (**Figure 5g**). A  
283 final type of structure recognized in these samples is the local development of packets of  
284 antigorite lamellae less than 500 nm in thickness, and elongated along the direction of  
285 cleavage (**Figure 5c** for instance), similar to those observed in deformed micas (e.g., Frey and  
286 Robinson, 1999).

287

#### 288 *Experiments with evidence for dehydration*

289 Two sets of deformation experiments were conducted under conditions above the thermal  
290 stability of antigorite (**Figure 1** and **Table 1**). Observations on the thin sections prepared from  
291 the recovered samples (DD58, DD59 and DD66) show various amounts of unreacted  
292 antigorites coexisting with small grains ( $\ll 1\mu\text{m}$  in size) of neoformed olivine (**Figure 4d**  
293 and **e**), which is a reaction product of the antigorite dehydration (see **Figure 1**). We consider  
294 the identification of neoformed olivine as necessary and sufficient evidence of dehydration.  
295 We did not observed enstatite or chlorite (to accommodate  $\text{Al}_2\text{O}_3$  excess in antigorite) nor  
296 "talc-like" crystals (Perrillat et al, 2005) that could be expected under these conditions;  
297 however, considering the small grain size of these new phases (a few tens of nanometers), we  
298 cannot exclude their presence. The occurrence of secondary olivine is particularly clear in  
299 DD66 (3,5 GPa, 650°C), indicating that dehydration occurred at lower temperature than that

300 indicated by the work of Ulmer and Trommsdorff (1995) for the corresponding experimental  
301 pressure. We thus confirm the updated curve proposed by Ulmer & Trommsdorff (1999) and  
302 also results from Hilairet et al (2006) (Figure 1). Optical observations in DD58 and DD59  
303 show that olivine represents less than 5% in volume of the samples, meaning that the amount  
304 of released water should be very low (<0.7 vol% overall), while sample DD66 displays ~50%  
305 of neoformed olivine. The distribution of olivine is clearly restricted to narrow domains  
306 (indicated by blue arrows in **Figure 4e**), suggesting that water from the dehydration reaction  
307 was released within the areas where olivine is observed, locally increasing the water/rock  
308 ratio and pore fluid pressure.

309         The analysis of the recovered samples also showed that a foliation did not develop  
310 either under these extreme conditions, and that the remaining antigorite preserves the original  
311 interpenetrative texture (**Figure 4d**). However, localized domains with significant CPOs of  
312 antigorite together with olivine grains develop perpendicularly as well as obliquely (about  
313 45°) to the compression direction, suggesting a more important contribution of plastic  
314 processes under these higher P-T conditions.

315         At the TEM scale, the decreased abundance of cataclastic textures in the dehydrated samples  
316 is the main difference with respect to those deformed within the stability field of antigorite,  
317 where these structures are common. Brittle structures are still present, however, and occur as  
318 microcracks that are locally decorated by neoformed grains of olivine along the open crack  
319 (**Figure 6a**). Such repartition of the byproducts of antigorite dehydration at the edge of the  
320 crack unambiguously links this microfracturing to dehydration. The olivine grains are  
321 almost xenomorphic in shape, ranging in grain size from a few tens of nanometers to a few  
322 tens of micrometers. In these samples we also observed that plastic structures are significantly  
323 more frequent in antigorite. We observed more abundant kinking (**Figure 6b**) and an increase  
324 of both the number of disordered antigorite crystals and of the amount of intracrystalline

325 disorder itself within these grains (**Figure 6c**). Antigorite lamellae are also found in the  
326 samples. **Figure 6d** shows a highly strained antigorite crystal, with dislocations putatively  
327 migrating and concentrating to create dislocation walls that can evolve into new grain  
328 boundaries (subgrain formation). This process may explain the formation of antigorite packets  
329 observed in all deformed samples. Locally, we also observed lattice orientations, but no  
330 preferential orientation shared within the whole sample. Finally, in the selected region  
331 prepared for TEM investigations in sample DD66, olivine is the main phase observed, and  
332 therefore it cannot be used to constrain the deformation behavior of antigorite.

333

### 334 **3.2. Naturally deformed samples**

335 Petrological examination of the samples collected from the eclogitic unit of the Escambray  
336 massif in Cuba (Cu12 and Cu24) show that they consist mainly of antigorite blades,  
337 unambiguously identified by Raman spectroscopy and TEM (Auzende et al, 2004). They  
338 display a visible foliation, attributed to eclogitic deformation (**Figure 7a**). However, the  
339 antigorite blades are mostly undeformed, as shown both by the shape of the blades and the  
340 clear and uniform extinction under cross-polarized light, indicating that antigorites have  
341 massively recrystallised under eclogitic conditions. In these samples, there is no evidence of  
342 antigorite breakdown, as no olivine is observed. Serpentinite Al24 is an antigorite mylonite  
343 deformed during the first steps of the burial of the Erro Tobbio series (Unit I), under  
344 conditions close to those of experiments DD60-DD61 (Hermann et al, 2000; Auzende et al,  
345 2006). Deformation manifests itself by the development of olivine-free shear bands (**Figure**  
346 **7b**). These three samples were naturally deformed under conditions that can be related to our  
347 non-dehydrated experiments.

348 Serpentinites Al19 and Al20, also collected in the Erro Tobbio unit (Unit III), were also  
349 deformed during the burial of this unit, but under more severe metamorphic conditions than

350 those of serpentinite A124. Indeed, they reach dehydration conditions (antigorite + brucite →  
351 olivine + water) resulting in the opening of veins filled with antigorite destabilisation  
352 products. Antigorite crystals are elongated along the foliation (**Figure 7c**). They are intensely  
353 sheared, and display undulatory extinction, characteristic of deformed crystals. This is  
354 confirmed by micrometric kink-bands visible under the light microscope. Veins filled with  
355 metamorphic olivine ± titanoclinohumite, resulting from the dehydration of antigorite, can be  
356 observed on metric outcrops (Hermann et al, 2000) as well as in thin sections (**Figure 7c**).  
357 These veins crosscut the foliation defined by the antigorite blades, and developed under  
358 eclogitic conditions that fall between those experimentally imposed for DD64-DD65 (no  
359 evidence of dehydration) and DD58-DD59 (appearance of metamorphic olivine).

360 At the TEM scale, we observe that natural samples display a greater amount of plastic  
361 structures (e.g., crystal disorder) compared to the experimentally deformed samples. In  
362 particular, approximately two-thirds of the crystals are highly disordered, and intracrystalline  
363 faults (stacking disorder, twinning, offset or dislocations) are very common, as illustrated on  
364 **Figure 8a and b**. This is particularly noticeable in the case of Erro Tobbio samples, where  
365 inherited antigorites have been highly sheared. In the Escambray massif samples, the density  
366 of defects in crystals is smaller. Antigorite commonly occurs as large oriented blades  
367 elongated along the foliation direction (**Figure 8e**), and display a modulation of dislocations  
368 that are scattered within the crystals, as shown on **Figure 8 b and g**. Minor chrysotile veins  
369 can be observed in most of the samples (**Fig. 8f**). In the Erro Tobbio samples it is also  
370 common to observe zones of recrystallisation at the interface between grains (**Figure 8c and**  
371 **d**), which were not observed in experimentally deformed samples. In a few cases we can  
372 document that the current grain boundary is a crack splitting an initial single crystal (**Figure**  
373 **8d, possibly 8c**), as previously shown by Auzende et al (2006). These brittle structures, while

374 not widespread in the naturally deformed samples, are significant. We did not observe any  
375 cataclastic textures in any of the investigated natural samples.

376 The main feature that can be identified within all investigated natural samples is the amount  
377 of intra-crystalline disorder. We observed a greater amount of crystal defects in highly  
378 sheared antigorites from all Erro-Tobbio samples compared to the less-sheared antigorite  
379 sampled in Cuba. We cannot observe any clear difference between samples deformed prior to  
380 or after water release from antigorite destabilization along the subduction path.

381

## 382 **4. Discussion**

383

### 384 *4.1. Lattice control of the deformation-induced microstructures in antigorite*

385 Microstructures from experimentally and naturally deformed serpentinites can be used to  
386 constrain how serpentinites accommodate deformation under high-pressure conditions (i.e.,  
387 subduction zone conditions). These microstructures are controlled by the crystallographic  
388 structure of serpentine, and the corrugated structure of antigorite (Figure 1-insert) likely  
389 promotes a different style of accommodation than typical to other phyllosilicates, such as  
390 lizardite (a flat serpentine variety) or micas. The brittle microstructures recognized in the  
391 investigated samples range from limited microcracking, affecting antigorite crystals (Figure  
392 5c), to cataclastic textures (Figure 5a and b). In all cases the crystal lattice of antigorite plays  
393 a major structural role. As with all serpentine minerals, antigorite is a phyllosilicate  
394 characterized by a layered structure and weak hydrogen bonding along the basal planes  
395 (Mellini, 1982). Thus, as expected, we noted that most of the cracks propagate along the (001)  
396 cleavage direction (Figure 5) and create new grains elongated along the two other  
397 crystallographic directions, as documented in deformed lizardite (Escartin et al, 1997; Viti &  
398 Hirose, 2009) or micas (Wong and Biegel, 1985). Such morphological control of the

399 deformed antigorite crystals, coupled to solid rotation of the grains to create a shape preferred  
400 orientation as a response to stress and deformation, should contribute to the strong CPO,  
401 namely the *c*-axis clustering observed in naturally foliated antigorite serpentinites (van de  
402 Moortele et al., 2010; Padrón-Navarta et al., 2012). Beside (001) delamination, intragranular  
403 microfractures that crosscut antigorite crystals (Figure 5c) can be explained by the relatively  
404 high strength of antigorite relative to other sheet silicates due to the layer reversals, with Si–  
405 O–Si bonds along  $c^*$  linking the layers (Kunze, 1956; Christensen, 2004). A significant  
406 proportion of these intracrystalline microfractures can be considered as features formed when  
407 the limit of plasticity of the material is reached, during kinking or bending (Figure 5d). This  
408 corresponds to a distinct type of intracrystalline fracturing, which can be interpreted as a  
409 response to a local accumulation of stress due to the lattice accommodation of the kinking.  
410 Indeed, kinking is characterized by migrating dislocations that increase the internal strain  
411 energy in the antigorite crystal (see Passchier and Trouw, 2005).

412 A distinct type of microcracks can unambiguously be attributed to dehydration of  
413 antigorite, as clearly established from figure 6a. These microcracks could be ascribed to  
414 hydraulic fracturing as proposed by Dobson et al (2002) as well as to antigorite  
415 embrittlement at the onset of the antigorite to olivine dehydration reaction (Jung et al, 2004).  
416 Both processes, while different, produce faulting and might be responsible for seismicity in  
417 subduction zones (Raleigh & Paterson, 1965; Peacock, 2001; Hacker et al, 2003; Omori et al,  
418 2004; Perillat et al, 2005). While we can hardly discuss further this issue, our results are  
419 similar, at smaller scale, to the observation reported by Jung et al (2004), who observed  
420 dehydration products of antigorite decorating surface of faults generated at high pressure.  
421 They suggested on this basis a weakening of the structure leading to faults initiating from the  
422 point where the reaction started and propagated. Fluids were evacuated while solid residue  
423 remained in place. Similar conclusions were proposed by Schubnel et al (2013) from the

424 germanate olivine to spinel transition, with fractures initiating at the onset of the reaction. On  
425 the other hand, dehydrated Erro Tobbio serpentinites show large olivine veins crosscutting  
426 antigorite foliation, supporting fluid-induced vein opening. While microfractures can also be  
427 observed in natural samples (Figure 8), they are largely healed and display evidence for  
428 recrystallization, making it difficult to systematically recognize them, and nearly impossible  
429 to attribute them to any specific deformation process. A recent paper by Chernak & Hirth  
430 (2011) proposes that weakening during dehydration is progressive and does not imply stick-  
431 slip instabilities required to explain seismicity. While our results show that dehydration and  
432 brittle behavior are clearly linked, we provide that the observation of the dehydration-induced  
433 microcracking alone does not necessitate that brittle deformation was unstable.

434 Plastic microstructures are also strongly controlled by the crystal structure of antigorite.  
435 Mainly, the (001) basal plane of antigorite, although reinforced by the strong Si-O-Si bonding  
436 between the layers at reversals, remains a weak plane that is likely to be the main slip surface.  
437 Thus, as expected for a phase with a preferential slip plane, antigorite develops kink bands  
438 (Figure 5 d to f). Kinking is well documented in the semibrittle deformation of talc close to  
439 dehydration conditions (Escartin et al, 2008) and is a common feature of phyllosilicate  
440 deformation (Paterson and Weiss, 1966; Shea and Kronenberg, 1992; Anderson, 2012).  
441 Recognized kink bands clearly show that basal slip can occur along both the *a* and *b*  
442 directions (Figure e and f respectively), meaning that two slip systems, (001)[010] and  
443 (001)[100], may be activated during the deformation event. Previous studies have proposed  
444 the dominant activation of either a single slip system of the latter (Hirauchi et al, 2010;  
445 Bezacier et al, 2010; van de Moortele et al, 2010) or of both (Padrón-Navarta et al, 2012),  
446 based on observations of CPO in naturally sheared serpentinites. Our study confirms that both  
447 slip systems are activated. Evidence for plastic gliding of the basal plane is also provided by  
448 the development of stacking disorder. Indeed, intracrystalline disorder in antigorite crystals

449 such as the occurrence of microtwinning, offsets, or other stacking faults, are mostly  
450 associated with glide of the (001) plane along  $a$  (Table 2). Finally, in naturally deformed  
451 samples, we observed recrystallization of antigorite, as previously reported by Auzende et al  
452 (2006). Recrystallization is attributed to a pressure solution process and has recently been  
453 confirmed by Padrón-Navarta et al. (2008; 2012) and Amiguet et al (2014) in naturally  
454 sheared serpentinites. Such a mechanism can accommodate deformation very efficiently, and  
455 is not directly controlled by the structure of antigorite, but by the porosity. However, as we  
456 discussed in the previous section, microcracking and the resulting porosity of antigorite  
457 serpentinite is largely controlled by its crystal structure, which indicates that pressure solution  
458 will also promote CPO in deformed serpentinites. This is in agreement with the conclusions  
459 of Katayama et al. (2009) who assume that the recorded seismic anisotropy parallel to the  
460 subduction trench is due to serpentine that deforms and generates geophysically observable  
461 CPO, although the authors infer dislocation creep as main deformation mechanism.

462

#### 463 *4.2. Semibrittle deformation and the influence of dehydration on plasticity*

464 The reported observations of experimentally and naturally deformed serpentinites clearly  
465 show the coexistence of both brittle and plastic deformation microstructures, pointing to a  
466 semi-brittle deformation regime for serpentinites under subduction zone conditions. At high  
467 pressure conditions, and within the stability field of antigorite, the significant proportion of  
468 highly fractured antigorite grains in the experimental samples suggests that most of the strain  
469 is accommodated by cataclastic deformation, and that plastic deformation only accommodates  
470 a small fraction of strain through basal gliding. Our results are in agreement with Chernak et  
471 al. (2010) who documented semibrittle deformation of antigorite at conditions relevant to  
472 subduction, as they reported faults and kink bands throughout their samples up to high  
473 temperature. Jung et al (2009) also detected acoustic emission characteristic of brittle

474 deformation within the stability field of antigorite; their samples were initially faulted and  
475 acoustic emissions were attributed to repeat frictional sliding along these preexisting faults.  
476 Here, we have confirmed these observations through the characterization of sample W1460,  
477 deformed at 1 GPa and 400°C, in which we recognized kink bands together with brittle  
478 features in the form of sample-scale faults accommodating a displacement of ~200  
479 micrometers, a type of localized deformation lacking in our D-DIA samples. We posit that our  
480 experiments document the same type of antigorite deformation described by Chernak et al.  
481 (2010), even though our samples did not display significant localization, probably due to  
482 differences in experimental set up, inhomogeneous deformation distribution, or both. We can  
483 also compare our results with those of Hilairet et al. (2007) from deformation of an antigorite  
484 sample under subduction zone conditions in a D-DIA apparatus. These experiments were  
485 conducted at similar strain rates but to a slightly lower total strain, and at 4GPa and 400°C, as  
486 they considered a colder geotherm (see Figure 1). Hilairet et al. (2007) discussed deformation  
487 mechanisms based on stress-strain curves obtained *in situ* with x-ray synchrotron analyses,  
488 and fitted their data with a dislocation creep power law. They assumed that antigorite  
489 accommodated deformation plastically, based on the absence of stress drops and on the  
490 apparent homogeneous deformation of the sample. While their data are consistent with an  
491 effective flow law, our microstructural observations suggests that this behaviour is likely not  
492 purely plastic, but attributable to distributed semibrittle deformation, with an important  
493 component of brittle deformation. Under these conditions strain localization is not efficient  
494 and deformation may proceed without significant stress drops. Also, as antigorite only has  
495 two easy slip systems - (001)[010] and (001)[100], it does not satisfy the von Mises criterion  
496 that requires five independent slip systems for plastic flow to occur homogeneously (von  
497 Mises, 1928). Thus, deformation by dislocation creep can hardly accommodate the total strain  
498 imposed on the samples, and requires other deformation mechanisms, as indicated by Padrón-

499 Navarta et al. (2012). Our conclusions are also consistent with the results by Escartin et al.  
500 (1997) who deformed antigorite under low-grade conditions (from 50 MPa to 1 GPa and  
501 room temperature) relevant to deformation of the oceanic lithosphere. The results from our  
502 study further support that deformation of antigorite from the subduction initiation down to  
503 antigorite breakdown depths (about 150 km) occurs in the semibrittle regime.

504 At conditions above the thermal stability of antigorite, we simultaneously observed an  
505 increase of plastic structures (greater intracrystalline disorder, recrystallization) together with  
506 a change in the nature of the brittle features. Indeed, cataclastic structures are lacking in  
507 dehydrating serpentinites and in several instances microcracks can unambiguously be linked  
508 to dehydration (Figure 6a). Although only a very small amount of H<sub>2</sub>O was released in the  
509 DD58 and DD59 samples due to dehydration, water locally promoted both plastic and brittle  
510 behaviour. We assume that while dehydration process promotes brittle behavior, as discussed  
511 in the previous section, aqueous fluid saturation together with higher temperature may have  
512 enhanced plasticity, as, for instance, previously observed in olivine (Mei and Kohlstedt, 2000;  
513 Jung and Karato, 2001). This plasticity manifests through higher crystal disorder of inherited  
514 crystals and recrystallisation due to pressure solution. While pressure solution is a direct  
515 result of water saturation, intracrystalline disorder should also be strongly enhanced by higher  
516 temperatures. We converge with Padrón-Navarta et al (2008) as they have also documented  
517 an increase of intracrystalline disorder in dehydrating antigorite from Cerro del Amirez and  
518 efficient pressure solution. The coexistence of brittle and plastic structures is also documented  
519 in dehydrating lizardite, as documented by Viti and Hirose (2009). This apparently diverges  
520 from the interpretation of Chernak and al. (2010) as they do not report brittle features in their  
521 samples deformed above antigorite breakdown. However, as we did not observed significant  
522 localization in our experimentally deformed samples displaying brittle microstructures, we

523 assume that a TEM investigation on Chernak's dehydrated samples may potentially reveal  
524 microcracks similar to those that we have observed.

525

#### 526 *4.3. Permeability and fluid migration in subduction zone*

527 A recent experimental study by Kawano et al (2011) has shown that antigorite serpentinite,  
528 under low confining pressure (50 MPa) at low temperature, and without deformation, has a  
529 very low permeability, among the lowest of metamorphic rocks, but noted a significant  
530 anisotropy of the permeability:  $10^{-22}$  m<sup>2</sup> when measured perpendicular to the foliation, and  
531 two orders of magnitude higher ( $10^{-20}$  m<sup>2</sup>) when measured parallel to it. We have shown that  
532 deformation at high pressure, under conditions relevant to subduction zones, produces  
533 microcracks and therefore porosity mostly along the basal planes of antigorite, likely as  
534 mixed-mode I-II microcracks (Escartin et al., 1997), and we thus expect that permeability  
535 would be greatly increased in the plane defined by cleavage, and that fluid circulation may be  
536 controlled by this anisotropic permeability structure. Indeed, this porosity can be  
537 interconnected, as microcracks should align in the same directions due to rigid rotation of the  
538 grains as response to the stress. This is supported by several studies that have shown that  
539 basal planes of antigorite are aligned with the foliation of natural serpentinites (van de  
540 Moortele et al, 2010; Padrón-Navarta et al, 2012). In subduction zones, Katayama et al (2009)  
541 propose that the observed trench-parallel anisotropy is due to serpentine deformation that  
542 results in antigorite basal cleavage (and foliation) is parallel to the subduction plane. Thus,  
543 oriented microcracking will enhance the percolation of aqueous fluids along the foliation  
544 direction (**Figure 9**), as suggested in prior studies (e.g., Escartin et al., 1997; Kawano et al.,  
545 2011). Also, intragranular microcracks observed in experimentally and naturally deformed  
546 samples (Figure 5c and 8d respectively) can allow fluid migration in directions across the  
547 foliation, and thus across the deformation zone (Figure 9).

548 In subduction zones, highly deformed serpentinites are commonly recognized in the  
549 serpentine channel above the subducting slab (e.g. Guillot et al, 2009). Katayama et al (2009)  
550 support this statement and emphasize the preferred orientation of antigorite crystals above the  
551 subducting slab, along the trench. Our results support the hypothesis that fluids likely migrate  
552 within the serpentinites, consistent with evidence for aqueous fluid percolation through these  
553 rocks, which include chrysotile veins as in Figure 8d (e.g., Andreani et al, 2007), and  
554 evidence for pressure solution as in Figure 8c (e.g., Auzende et al, 2006; Padrón-Navarta et al,  
555 2012). Geochemical observations also point toward aqueous fluids in the subducting  
556 serpentinites. Indeed, Deschamps et al (2013) proposed that the observed enrichment of light  
557 rare earth elements in subducted serpentinites could be ascribed to sedimentary-derived fluid  
558 interacting with rock within the subduction channel after the serpentinization. Thus, all these  
559 observations suggest that in spite of low permeability measured experimentally at the sample  
560 scale and under static conditions (Kawano et al, 2011), aqueous fluids in the subduction  
561 system seem to rather efficiently percolate in the serpentinite. This percolation likely allows  
562 the development of the thin hydrated serpentine layer above the subducting slab due to the  
563 buoyant ascent of the fluids via an oriented connected porosity network (i.e., along the  
564 foliation), and also leading to the hydration of the mantle wedge through water transport  
565 across the foliation of the deformation zone (Figure 9). This across-foliation water transport is  
566 likely to be significantly less efficient than the along-foliation, owing to the nature of brittle  
567 deformation processes described above, and operate throughout the subduction zone.

568

#### 569 *4.4. Input of the comparison between Nature and experiments on deformation of antigorite* 570 *during subduction*

571 All our observations of natural and experimental samples indicate that antigorite  
572 serpentinites deforms in the semibrittle regime up to its complete dehydration. Optically, the

573 main difference between naturally and experimentally deformed antigorite serpentinites is the  
574 presence of a penetrative foliation in the former that was induced by deformation, which is  
575 not observed in experimental samples. Yet, at the TEM scale, both types of samples reveal  
576 both brittle and plastic structures. In experiments conducted within the stability field of  
577 antigorite, it has been shown that cataclastic flow controls the rheological behaviour of  
578 serpentinite, while microstructures in natural samples instead suggest a significant  
579 contribution of plasticity, with a foliation indicative of more homogeneous deformation. The  
580 absence of foliation and lesser contribution of plasticity in experimental samples can surely be  
581 attributed to i) the higher strain rates during experimental deformation ( $5 \times 10^{-5}$  and  $1 \times 10^{-4}$   
582 during D-DIA experiments compared to  $10^{-12}$  -  $10^{-14}$  s<sup>-1</sup> in nature), ii) to the limited strains  
583 achieved in experiments that do not allow a steady state flow (a few percent shortening in the  
584 laboratory and extremely high values in the field), as stated by Chernak et al (2010), and iii)  
585 to the absence of fluids promoting syntectonic growth that likely takes place in natural shear  
586 zones within the subduction zone. Also, most experimental samples are deformed in axial  
587 compression while natural samples are typically deformed under simple shear. This means  
588 that experimental results cannot be used to constrain the conditions under which this foliation  
589 develops in nature, as such processes cannot be replicated in laboratory experiments at the  
590 moment. Nonetheless, while low strain rates may be responsible for foliation developement,  
591 we assume that brittle features recognized in natural samples can be attributed to higher strain  
592 rates events that may or may not have a seismic origin, as stated by Chernak & Hirth (2011).

593         The presence of aqueous fluids derived from the dehydration of other hydrous phases  
594 during burial (see Poli and Schmidt, 1998) in natural samples subducted and exhumed under  
595 conditions below antigorite breakdown can be suggested by the presence of chrysotile veins  
596 (Figure 8b) or indication of pressure solution evidence (Figure 8c), as both structures require  
597 the presence of fluids. The significant amount of plastic microstructures in natural samples

598 can also be promoted by the presence of aqueous fluids together with higher temperature,  
599 even under conditions below antigorite breakdown. This is supported by the greater amount  
600 of plastic structures in experimentally dehydrated samples. We thus conclude that brittle  
601 deformation in subduction zones is likely associated with high strain-rate events such as  
602 deformation associated with seismicity, occurring from throughout the subduction zone from  
603 the surface to the depth of antigorite breakdown. Plastic deformation developing foliation  
604 likely occurs at lower strain rates and under water saturation. Semi brittle deformation of  
605 antigorite can thus potentially generate a permeability network throughout the subduction  
606 system, with efficient transport along the deformation zone, and more limited one across it.

607

## 608 5. Conclusions

609 This work presents detailed microstructural observations to determine the mode of  
610 deformation in both experimentally and naturally deformed samples at subduction conditions,  
611 and near antigorite breakdown. Our results show that:

612 - Antigorite deforms in the semibrittle regime at high pressure. Brittle deformation in  
613 subduction zones is likely associated with high strain-rate events, including seismic events  
614 and can overimprint low strain-rate plastic deformation microstructures.

615 - The relative importance of brittle deformation relative to plastic deformation is likely  
616 promoted by a combination of the presence of water (elevated pore fluid pressures and  
617 dehydration), higher temperature and elevated strain rates.

618 - The crystal lattice structure of antigorite favours microcracking along (001), which promotes  
619 interconnected porosity along the foliation direction in subduction zones. Antigorite structure  
620 also induces significant intragranular fracturing. Semibrittle deformation can thus sustain a  
621 permeable deformation zone down to the level of antigorite dehydration.

622 - Owing to a likely anisotropic permeability network, aqueous fluids may migrate more  
623 efficiently along the surface of the subducting slab than across it, exploiting the microporosity  
624 developed along the foliation during brittle deformation events. Across-deformation zone  
625 migration may be facilitated through intragranular fracturing, resulting in an upward  
626 migration towards the mantle wedge above the subduction plane allowing its hydration.

627

628 **Acknowledgements:** The authors wanted to thank J.A. Padrón-Navarta and a second  
629 reviewer for their great work reviewing this manuscript. We are also grateful to the BGI  
630 Bayreuth technical staff for assistance with the preparation of the recovered samples. This  
631 work was supported by PNP and SYSTER Program (INSU/CNRS) and BGI "IHP Access to  
632 Research Infrastructure program. G. Hirth was supported by National Science Foundation  
633 grant EAR-0810188 for experiment W1460 used in this study.

634

635

636

637  
638

**Table 1** : Experimental conditions for D-DIA and Griggs runs, and metamorphic conditions undergone by natural samples

<i>Experimentally-deformed serpentinites</i>						
Sample	P (Gpa)*	T (°C)*	Strain rate	Total strain	dehydration evidence	Ref
DD60	1.0	400	5×10 <sup>-5</sup>	24%	none	This study
DD61	1.0	400	1×10 <sup>-4</sup>	26%	none	This study
DD63	1.8	550	-	static	none	This study
DD64	1.8	550	1×10 <sup>-4</sup>	28%	none	This study
DD65	1.8	550	5×10 <sup>-5</sup>	27%	none	This study
DD58	2.5	650	1×10 <sup>-5</sup>	8%	olivine	This study
DD59	2.5	650	1×10 <sup>-4</sup>	26%	olivine	This study
DD66	3.5	650	5×10 <sup>-5</sup>	30%	olivine	This study
W1460	1.0	400	1.5×10 <sup>-5</sup>	33%	none	Chernak et al, 2010
<i>Naturally sheared serpentinites</i>						
Sample	P (GPa)	T (°C)	Origin		dehydration evidence	Ref
Cu12 / Cu24	1.2 ± 2	450 ± 30	Escambray, Cuba		none	Auzende et al, 2004
Al24 (ET1)	0.9 ± 3	360 ± 60	Erro Tobbio, Alps		none	Hermann et al, 2000
Al19 / Al20 (ET3)	2.0 ± 2	600 ± 40	Erro Tobbio, Alps		ol + TiCl	Hermann et al, 2000

639 \* errors are estimated according to Wang et al (2003) - T ± 20°C, P ± 10%

640

641

642

643

644

645

646 **Table 2** : Description of the deformation-linked microstructures observed in antigorite  
 647 serpentinites (from Otten, 1993; Gorbety, 2003; Passchier & Trouw, 2005)

648

Type of microstructure	Abbreviation	Description
Decompression cracks	Decomp.	Cracks due to the decompression of the assembly after temperature quench
Shear band	SB	Wavy ductile structure which localize intense strain. Common in phyllites
Kink band	KB	Tabular fold zones due to slipping of basal planes and resulting from shear couple
Microcracks	$\mu$ C	Brittle planar discontinuity, commonly with some dilatation. High density of microcracking can lead to through-going fault
Dislocation wall	DW	Intracrystalline planar zone that concentrate migrating dislocations. Can evolve to a neoformed grain boundary (GB)
Offset	O	Lateral gliding of the layers (along $a$ ) due to the shift of the tetrahedral reversal from TO layer to the other by one tetrahedron position
Twinning	Tw	Mirror operation along the basal plane coupled to a gliding of the layer of $a/2$ . The modulations are thus shifted of half a wavelength
Two-layer polytype	2L-P	Combination of twinning or offset can lead to a 1.4 nm periodicity in the $c^*$ direction instead of 0.7 nm typical of antigorite
Stacking defect	SD	All other possible types of stacking defects (or unrecognized)
Modulation dislocation	MD	Termination of antigorite waves on modulation dislocations.
Recrystallisation	R	Zones of recrystallisation attributed to pressure solution processes

649

650

651 **Figure captions**

652 **Figure 1** : P-T diagram plotting the experimental conditions reported in this study and from  
653 previous experimental works. Curve limiting the thermal stability of antigorite are reported  
654 from Ulmer & Trommsdorff (1999) and Hilairet et al (2006). We also reported the curve  
655 from Ulmer & Trommsdorff (1995) which is widely used in the litterature but is incorrect (see  
656 Ulmer & Trommsdorff, 1999). We also plotted the metamorphic conditions undergone by  
657 natural samples (ET1, 2 and 3 correspond to Erro-Tobbio metamorphic stages from Hermann  
658 et al, 2000; VM, PG and LG stand for Vizzo Mozzo, Passo Gallarino and Lago Superiore  
659 units described by Schwartz et al, 2000) as well as experimental conditions from previous  
660 studies. Insert illustrates to the corrugated crystal structure of antigorite (dark silicate  
661 tetrahedra and light magnesian octahedra)

662

663 **Figure 2.** a) schematic representation of the assembly prepared for the D-DIA experiment,  
664 and b) photography of the assembly, c) the assembly monted in the D-DIA, d) optical  
665 microscopy image of a recovered sample (DD59)

666

667 **Figure 3.** a) Starting material image under cross polarized light showing interpenetrative  
668 texture of antigorite (Atg) serpentinite, b) TEM micrograph of crosscutting antigorite blades  
669 from the starting material. c) natural light / cross polarized light mounted image of sample  
670 DD63 (static run) showing decompression-induced fractures (Decomp).  $\sigma_1$  is horizontal.

671

672 **Figure 4.** Optical microphotographs of recovered samples from non-dehydrated and  
673 dehydrating experiments.  $\sigma_1$  is vertical on all images except b where it is rotated of  $90^\circ$ . a)  
674 typical interpenetrative texture inherited from the starting material (DD65), b) oblique  
675 localized damaged zone crosscutting the sample (DD61), c) fault crosscutting W1460  
676 (Chernak et al, 2010), d) Secondary micrograins of olivine associated to antigorite underline  
677 the significant dehydration of DD66, e) dehydrated samples showing local concentration of  
678 inframironic grains of olivine (showed by blue arrows) (DD59).

679

680 **Figure 5.** TEM bright field microcrographs of recovered samples from non-dehydrated  
681 experiments. a) and b) show cataclastic textures with antigorite grains cracking preferentially  
682 along (001) cleavage (Cl), c) intracrystalline microcracks propagating through an antigorite  
683 crystal. Antigorite lamellae can be recognized, d, e and f) antigorite crystal showing kink

684 bands (KB), with a gliding of the basal planes along  $a$  direction (d and e) and  $b$  (f). Antigorite  
685 shown on f) is observed along  $\langle 100 \rangle$  and can be discriminated from lizardite on SAED pattern  
686 by slight tilting the crystal and revealing surstructure diffraction spots (DW = dislocation wall),  
687 g) bright field and associated SAED pattern of an ordered antigorite, h) bright field and  
688 associated SAED pattern of a slightly disordered antigorite showing twinning (Tw) and  
689 stacking defects (SD).

690

691 **Figure 6.** TEM bright field microcrographs of recovered samples from dehydrating  
692 experiments a) and associated SAED pattern showing olivine grains (Ol) decorating the edges  
693 of a microcrack, b) and associated SAED pattern showing kinked antigorite, c) and associated  
694 SAED pattern showing highly disordered antigorite. Staking disorder is emphasized on the  
695 SAED pattern by the presence of diffuse streaks along  $c^*$ , d) antigorite crystal showing  
696 migrating dislocation walls (DW) that may evolve to grain boundary (GB)

697

698 **Figure 7.** Optical microphotographs of naturally sheared serpentinite samples. a) antigorite  
699 serpentinite Cu12 from the Escambray massif (Cuba). Foliation is underlined by slightly  
700 deformed antigorite blades, highly sheared antigorite mylonite from b) unit I of Erro Tobbio  
701 (Alps) showing shear bands (SB), and c) from unit III of Erro Tobbio (Alps) showing  
702 plurimicronic kink bands and veins filled with by products of antigorite dehydration olivine et  
703 Titano-clinohumite

704

705 **Figure 8.** TEM bright field microcrographs of naturally sheared serpentinites showing a) high  
706 intracrystalline disorder, as observed on the micrograph and associated SAED pattern, b) high  
707 resolution image of a slightly disorder antigorite crystal with a modulation dislocation (D), c)  
708 microcrack healed by recrystallisation (R) due to pressure solution, d) microcrack with little  
709 recrystallisation, e) elongated antigorite blades, f) chrysotile veins inherited from the oceanic  
710 event or produced during fluid migration in subduction context, g) antigorite seen along  
711  $\langle 001 \rangle$  showing modulation dislocation

712

713 **Figure 9.** Schematic cartoon of a subduction zone (redrawn after Hilairet & Reynard, 2009  
714 and Kawano et al, 2011). Two isotherms are represented (1100 and 1400°C). The green  
715 region correspond to the serpentinitized mantle, the dotted line represent the antigorite  
716 breakdown conditions and and the blue arrows represent the putative migration paths of the  
717 fluids produced by sediment dehydration. Insert : Magnification of the serpentine channel

718 above the subducting slab. Fluids can migrate mostly parallel to the foliation, promoting the  
719 formation of the serpentized layer above the subducting slab. They can also migrate  
720 upwards and hydrate the mantle wedge and contribute to arc magmatism through  
721 intracrystalline microcracks.

722

## 723 REFERENCES

- 724 Agard, P., Yamato, P., Jolivet, L., Burov E., 2009. Exhumation of oceanic blueschists and  
725 eclogites in subduction zones: Timing and mechanisms. *Earth Sci. Rev.* 92, 53-79. DOI:  
726 10.1016/j.earscirev.2008.11.002.
- 727 Amiguet, E., Van de Moortele, B., Cordier, P., Hilairet, N., Reynard, B., 2014. Deformation  
728 mechanisms and rheology of serpentines in experiments and in nature. *J. Geophys. Res.*  
729 4640-4654.
- 730 Andreani, M., Mevel, C., Boullier, A-M., Escartin, J., 2007. Dynamic control on serpentine  
731 crystallization in veins: Constraints on hydration processes in oceanic peridotites. *Geoch.*  
732 *Geophys. Geosyst.* 8, Q02012. DOI: 10.1029/2006GC001373.
- 733 Angiboust, S., Langdon, R., Agard, P., Waters, D., Chopin, C., 2011. Eclogitization of the  
734 Monviso ophiolite and implications on subduction dynamics. *J. Metam. Geol.* 30, 37–61.
- 735 Auzende, A.L., Guillot, S., Devouard, B., Baronnet, A., 2006. Behaviour of serpentinites in  
736 convergent context : Microstructural evidence. *Eur. J. Mineral.* 18, 21-33.
- 737 Auzende, A-L., Daniel, I., Reynard, B., Lemaire, C., Guyot, F., 2004. High-pressure  
738 behaviour of serpentine minerals: a Raman spectroscopic study. *Phys. Chem. Mineral.* 31,  
739 269-277. DOI 10.1007/s00269-004-0384-0.
- 740 Auzende, A-L., Devouard, B., Guillot, S., Daniel, I., Baronnet, A., Lardeaux, J-M., 2002.  
741 Serpentinites from Central Cuba: petrology and HRTEM study. *Eur. J. Mineral.* 14, 905-  
742 914.
- 743 Bezacier, L., Reynard, B., Bass, J., Sanchez Valle, C., van de Moortele, B., 2010. Elasticity of  
744 antigorite, seismic detection of serpentinites, and anisotropy in subduction zones. *Earth*  
745 *Planet. Sci. Lett.* 289, 198-208.
- 746 Chernak, L.J., Hirth, G., 2010. Deformation of antigorite serpentinite at high temperature and  
747 pressure. *Earth Planet. Sci. Lett.* 296, 23-33.

748 Chernak, L.J., Hirth, G., 2011. Syndeformational antigorite dehydration produces stable fault  
749 slip. *Geology* 39, 847-850. doi:10.1130/G31919.1.

750 Christensen, N.I., 2004. Serpentinites, peridotites and seismology. *Int. Geol. Rev.* 46:795-816.

751 Deschamps, F., Godard, M., Guillot, S., Hattori, K.H., 2013. Geochemistry of subduction zones  
752 serpentinites: A review. *Lithos*, doi: 10.1016/j.lithos.2013.05.019.

753 Dobson, D.P., Meredith, P.G., Boon, S.A., 2002. Simulation of subduction zone seismicity by  
754 dehydration of serpentine. *Science*, 298, 407-1410.

755 Escartin, J., Hirth G., 1997. Non dilatant brittle deformation of serpentinites: Implications for  
756 Mohr-Coulomb theory and the strength of faults. *J. Geophys. Res.* 102, 2897-2913.

757 Escartin, J., Andreani, M., Hirth, G., Evans, B., 2008. Relationships between the  
758 microstructural evolution and the rheology of talc at elevated pressures and temperatures.  
759 *Earth Planet. Sci. Lett.* 268, 463-475. DOI: 10.1016/j.epsl.2008.02.004.

760 Frey, M., Robinson, D., 1999. Low grade metamorphism. Backwell Sci Ltd pp313.

761 Fryer, P., Wheat, C.G., Mottl, M.J., 1999. Mariana blueschist mud volcanism: Implications for  
762 conditions within the subduction zone. *Geology* 27, 103-1999. DOI: 10.1130/0091-  
763 7613(1999)027<0103:MBMVIF>2.3.CO;2.

764 Garth, T., Rietbrock, A., 2014. Order of magnitude increase in subducted H<sub>2</sub>O due to  
765 hydrated normal faults within the Wadati-Benioff zone. *Geology* 42, 207–210.

766 Grobety, B., 2003. Polytypes and higher-order structures of antigorite : A TEM study. *Am*  
767 *Mineral* 88, 27-36.

768 Guillot, S., Agard, P., Schwartz, S., Vidal, O., 2009. Exhumation processes in oceanic and  
769 continental subduction contexts: A review In: Lallemand S, Funiciello F (Eds) *Frontiers in*  
770 *Earth Science*, 175-205. doi: 10.1007/978-3-540-87974-9\_10.

771 Guillot, S., Hattori, K.H., de Sigoyer, J., Nagler, T., Auzende, A.L., 2001. Evidence of  
772 hydration of the mantle wedge and its role in the exhumation of eclogites. *Earth Planet.*  
773 *Sci. Lett.* 193, 115-127.

774 Hacker, B.R., Peacock, S.M., Abers, G.A., Holloway, S.D., 2003. Subduction factory - 2. Are  
775 intermediate-depth earthquakes in subducting slabs linked to metamorphic dehydration  
776 reactions? *J. Geophys. Res.* 108:B1203. DOI: 10.1029/2001JB001129.

777 Hirauchi, K.I., Katayama, I., Uehara, S., Miyahara, M., Takai, Y., 2010. Inhibition of  
778 subduction thrust earthquakes by low temperature plastic flow in serpentine. *Eart Planet. Sci.*  
779 *Lett.* 295, 349-357. DOI: 10.1016/j.epsl.2010.04.007

780 Hirth, G., Guillot, S., 2013. Rheology and tectonic significance of serpentinite. *Elements* 9.  
781 doi: 10.2113/gselements.9.2.95.

782 Hermann, J., Müntener, O., Scambelluri, M., 2000. The importance of serpentine mylonites  
783 for subduction and exhumation of oceanic crust. *Tectonophysics* 327, 225-238.

784 Hilairet, N., Daniel, I., Reynard, B., 2006. Equation of state of antigorite, stability field of  
785 serpentines, and seismicity in subduction zones. *J. Geophys. Res.* 83: L02302.  
786 doi:10.1029/2005GL024728.

787 Hilairet, N., Reynard, B., 2009. Stability and dynamics of serpentinite layer in subduction  
788 zone. *Tectonophysics* 465, 24-29. DOI: 10.1016/j.tecto.2008.10.005.

789 Hilairet, N., Reynard, B., Wang, Y., Daniel, I., Merkel, S., Nishiyama, N., Petitgirard, S.,  
790 2007. High-pressure creep of serpentine, interseismic deformation and initiation of  
791 subduction. *Science* 318, 1910-1913.

792 Hyndman, R.D., Peacock, S.M., 2003. Serpentinization of the forearc mantle. *Earth Planet.*  
793 *Sc. Lett.* 212, 417-432.

794 Jung, H., Karato, S., 2001. Water induced fabric transitions in olivine. *Science* 293, 1460-  
795 1463.

796 Jung, H., Green, H.W., Dobrzhinetskaya, F., 2004. Intermediate-depth earthquake faulting by  
797 dehydration embrittlement with negative volume change. *Nature* 428, 545-549

798 Jung, H., Green, H.W., 2004. Experimental Faulting of Serpentinite during Dehydration:  
799 Implications for earthquakes, Seismic Low-Velocity Zones, and Anomalous Hypocenter  
800 Distributions in Subduction Zones. *Internat. Geol. Rev.* 46, 1089-1102.

801 Jung, H., Fei, Y., Silver, P., Green, H.W., 2009). Frictional sliding in serpentine at very high  
802 pressure: *Earth Planet. Sci. Lett.* 277: 273–279, doi:10.1016/j.epsl.2008.10.019.

803 Kamiya, S., Kobayashi, Y., 2000. Seismological evidence for the existence of serpentinitized  
804 mantle wedge. *Geophys. Res. Lett.* 27, 819-822.

805 Katayama, I., Hirauchi, K.I., Michibayashi, K., Ando, J.I., 2009. Trench-parallel anisotropy  
806 produced by serpentine deformation in the hydrated mantle wedge. *Nature* 461, 1114-1117

807 Kawano, S., Katayama, I., Okazaki, K., 2011. Permeability anisotropy of serpentinite and  
808 fluid pathways in subduction zones. *Geology* 39, 939-942.

809 Kunze, G., 1956. Die gewellte struktur des antigorits, I. *Zeitsch Kristall* 108, 82-107.

810 Marchesi, C., Garrido, C.J., Padrón-Navarta, J.A., López Sánchez-Vizcaíno, V., Gómez-  
811 Pugnaire, M.T., 2013. Element mobility from seafloor serpentinization to high-pressure  
812 dehydration of antigorite in subducted serpentinite: Insights from the Cerro del Almirez  
813 ultramafic massif (southern Spain). *Lithos* 15, 128-142.

814 Mei, S., Kohlstedt, D.L., 2000a. Influence of water on plastic deformation of olivine  
815 aggregates. 1. Diffusion creep regime. *J. Geophys. Res.* 105, 21457-21469

816 Mei, S., Kohlstedt, D.L., 2000b. Influence of water on plastic deformation of olivine  
817 aggregates. 2. Dislocation creep regime. *J. Geophys. Res.* 105, 21471-21481

818 Mellini, M., 1982. The crystal structure of lizardite-1T: hydrogen bonds and polytypism. *Am.*  
819 *Mineral.* 67, 587-598.

820 Mevel, C., 2003. Serpentinization of abyssal peridotites at mid-ocean ridges. *C. R. Geosc.*  
821 335, 825-852.

822 Omori, S., Komabayashi, T., Maruyama, S., 2004. Dehydration and earthquakes in the  
823 subducting slab: empirical link in intermediate and deep seismic zones. *Phys. Earth*  
824 *Planet. Int.* 146, 297-311.

825 Otten, M.T., 1993. High-resolution transmission electron-microscopy of polysomatism and  
826 stacking defects in antigorite. *Am. Mineral.* 78,75-84.

827 Padrón-Navarta, J.A., Tommasi, A., Garrido, C.J., Lopez Sanchez, V., 2012. Plastic  
828 deformation and development of antigorite crystal preferred orientation in high-pressure  
829 serpentinites. *Earth Planet. Sci. Lett.* 349-350, 75-86.

830 Padrón-Navarta, J.A., Tommasi, A., Garrido, C.J., Lopez Sanchez, V., Gomez-Pugnaire,  
831 M.T., Jabaloy, A., Vauchez, A., 2010. Fluid transfer into the wedge controlled by high-  
832 pressure hydrofracturing in the cold top-slab mantle. *Earth Planet. Sci. Lett.* 297, 271-286.

833 Padrón-Navarta, J.A., López Sánchez-Vizcaíno, V., Garrido, C.J., Gómez-Pugnaire, M.T.,  
834 Jabaloy, A., Capitani, G., Mellini, M., 2008. Highly ordered antigorite from Cerro del

835 Almirez HP-HT serpentinites, SE Spain. *Contributions to Mineralogy and Petrology* 156,  
836 679-688

837 Passchier, C.W., Trouw, R.A., 2005. *Microtectonics*, Springer, Berlin

838 Paterson, M.S., Weiss, L.E., 1966. Experimental deformation and folding in phyllite. *Geol.*  
839 *Soc. Am. Bull.* 77, 343-374. DOI: 10.1130/0016-7606(1966)77[343:EDAFIP]2.0.CO;2

840 Peacock, S.M., 2001. Are the lower planes of double seismic zones caused by serpentine  
841 dehydration in subducting oceanic mantle. *Geology*, 29, 299-302.

842 Perrillat, J.P., Daniel, I., Koga, K.T., Reynard, B., Cardon, H., Crichton, W.A., 2005. Kinetics  
843 of antigorite dehydration: A real-time diffraction study. *Earth Planet. Sci. Lett.* 236, 899-  
844 913. DOI: 10.1016/j.epsl.2005.06.006.

845 Reynard, B., 2013. Serpentine in active subduction zones. *Lithos* 178, 171-185.

846 Scambelluri, M., Muntener, O., Hermann, J., Piccardo, G.B., Trommsdorff, V. (1995)  
847 Subduction of water into the mantle: history of an alpine peridotite. *Geology* 23, 459-  
848 462.

849 Schmidt, M.W., Poli, S., 1998. Experimentally based water budgets for dehydrating slabs and  
850 consequence for arc magma generation. *Earth Planet. Sci. Lett.* 163, 361-379. DOI:  
851 10.1016/S0012-821X(98)00142-3.

852 Schwartz, S., Lardeaux, J.M., Guillot, S., 2000. The diversity of eclogitic metamorphism in  
853 the Monviso ophiolitic complex, western Alps, Italy. *Geodyn. Acta.* 13, 169-188.

854 Shea, W.T., Kronenberg, A.K., 1992. Rheology and deformation mechanisms of an isotropic  
855 mica schist. *J. Geophys. Res.* 97, 15201-15237.

856 Spear, F.S., 1995. *Metamorphic Phase Equilibria and Pressure-Temperature-Time Paths.*  
857 *Mineral. Soc. Am., Mon Ser* pp799.

858 Tatsumi, Y., Kogiso, T., 2003. The subduction factory: Its role in the evolution of the earth's  
859 crust and mantle. *Geol. Soc. London Spec. publ.* 2003 219:55-80. doi:  
860 10.1144/GSL.SP.2003.219.01.03.

861 Ulmer, P., Trommsdorff, V., 1999. Phase relations of hydrous mantle subducting to 300 km,  
862 in: Fei Y, Bertka CM, Mysen BO (Eds) *Mantle Petrology: Field observations and high*  
863 *pressure experimentations.* The Geochemical Society, pp259-281.

864 Ulmer, P., Trommsdorff, V., 1995. Serpentine stability to mantle depths and subduction-  
865 related magmatism. *Science* 268, 858-861.

866 van de Moortele, B., Bezacier, L., Trullenque, G., Reynard, B., 2010. Electron back-scattering  
867 diffraction (EBSD) measurements of antigorite lattice-preferred orientations (LPO). *J.*  
868 *Microsc.* 239, 245-248.

869 van Keken, P., 2003. The structure and dynamics of the mantle wedge. *Earth Planet. Sci.*  
870 *Lett.* 215, 323-338.

871 Viti, C., Hirose, T., 2009. Dehydration reactions and micro/nanostructures in experimentally-  
872 deformed serpentinites. *Contrib. Mineral. Petrol.* 157, 327-338.

873 von Mises, R., 1928. Mechanics of the ductile form changes of crystals. *Zeits. Angewan.*  
874 *Math. Mech.* 8, 161-185.

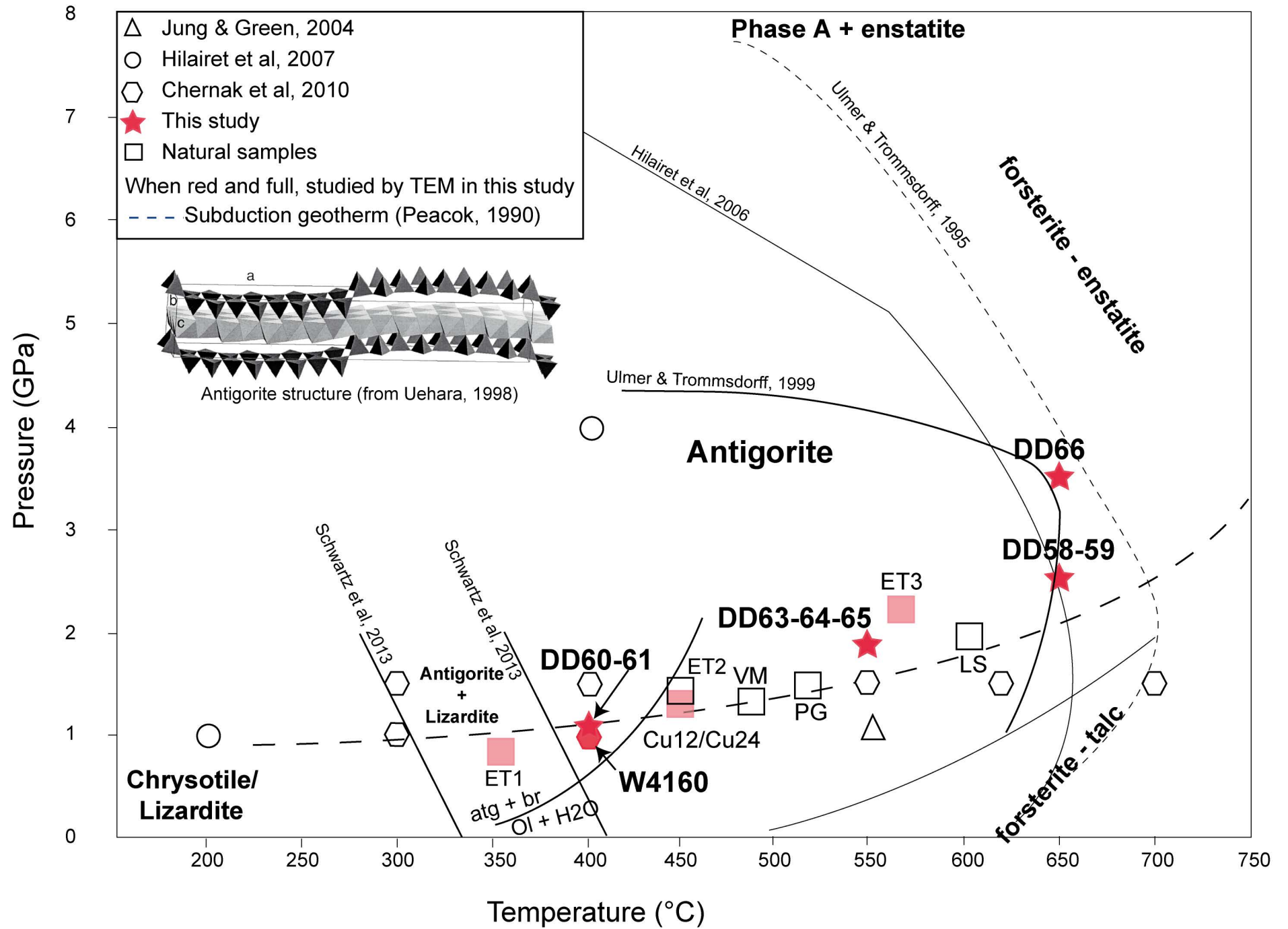
875 Wada, I., Wang, K., He, J., Hyndman, R., 2008. Weakening of the subduction interface and  
876 its effects on surface heatflow, slab dehydration, and mantle wedge serpentinization. *J.*  
877 *Geophys. Res.* 113, B04402. doi:10.1029/2007JB005190.

878 Wang, Y., Durham, W.B., Getting, I.C., Weidner, D.J., 2003. The deformation-DIA: A new  
879 apparatus for high temperature triaxial deformation to pressures up to 15 GPa. *Rev. Sci.*  
880 *Instrum.* 74, 3002-3011.

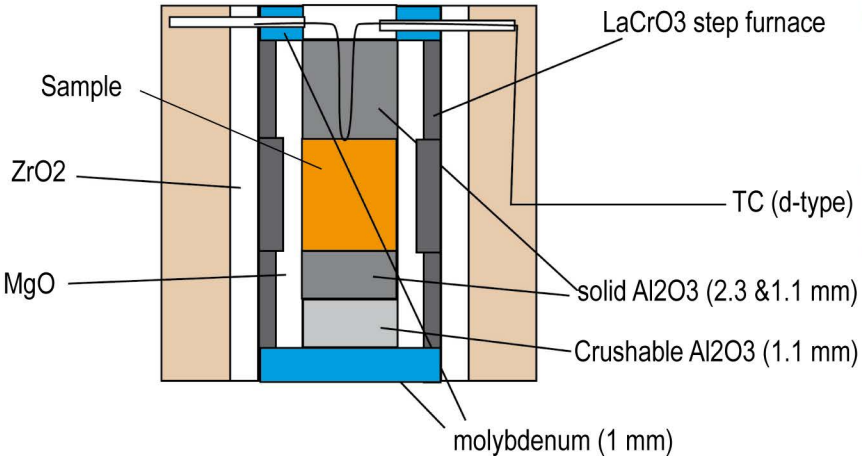
881

882

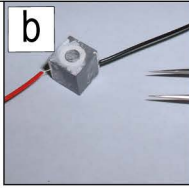
883



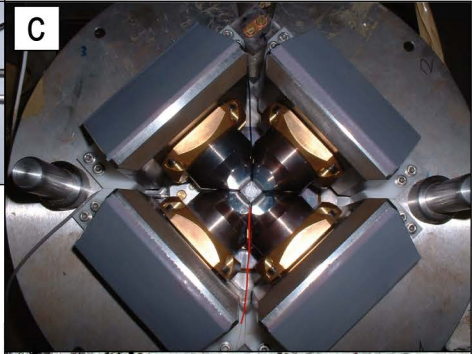
a



b



c



d



